Nuclear Materials and Energy 18 (2019) 111–117

Contents lists available at ScienceDirect

Nuclear Materials and Energy

journal homepage: www.elsevier.com/locate/nme

3D simulations of turbulent mixing in a simplified slab-divertor geometry

N.R. Walkden[a,*], F. Riva[a], B.D. Dudson[b], C. Ham[a], F. Militello[a], D. Moulton[a], T. Nicholas[a,b], J.T. Omotani[a]

[a] CCFE-UKAEA, Culham Science Centre, Abingdon, Oxfordshire, OX14 3DB, UK
[b] York Plasma Institute, University of York, Heslington, York, YO10 5DD, UK

ABSTRACT

Three-dimensional simulations of plasma turbulence have been run using the STORM module of BOUT + + in a simple slab geometry aimed at representing a single, isolated tokamak divertor leg. Turbulence is driven primarily by the Kelvin-Helmholtz mechanism due to the sheared ExB flow that forms around the separatrix due to strong radial gradients in the sheath potential which arise from strong radial gradients in the electron temperature. The turbulence forms a mixing layer around the separatrix which spreads heat and particles into the private-flux region. The resulting spread of the electron heat flux is within the experimental range measured on MAST. An effective thermal transport coefficient which is approximately 10% of the Bohm value is measured from the simulations. When a transport coefficient of this magnitude is used in a diffusive axisymmetric simulation, the time-averaged radial profiles share similar features to the full turbulence simulation.

1. Introduction

The flux of heat and particles to the divertor surface is an important quantity for the operation of tokamak devices. Excessive fluxes may limit machine operation by damaging the surface of the divertor, whilst a precise knowledge of these fluxes allows for better estimation of material erosion rates. Many aspects of tokamak operation are dependent on knowledge of profiles at the divertor target, which in turn depend on the competition between perpendicular and parallel transport processes in the scrape-off layer. Whilst parallel transport processes are relatively well captured in two-dimensional axisymmetric fluid transport codes such as SOLPS [1,2], perpendicular transport remains more difficult to account for due to its turbulent nature. In broad terms, the contribution of perpendicular transport to profiles at the divertor surface can be decoupled into processes upstream that populate the SOL with particles and heat, and processes downstream that spread these particles and heat across magnetic fieldlines either further into the SOL or into the private-flux region (PFR). This idea is encapsulated in the Eich function [3]

$$q(s) = \frac{q_0}{2}\exp\left(\left(\frac{S}{2\lambda_q}\right)^2 - \frac{x_t}{\lambda_q f_x}\right) erfc\left(\frac{S}{2\lambda_q} - \frac{x_t}{S f_x}\right) + q_{bg} \quad (1)$$

where the upstream and downstream transport processes are captured in the λ_q and S parameters respectively. x_t is the radial coordinate at the target, centred on the separatrix; q_0 and q_{bg} are the peak and background heat fluxes respectively and f_x is the midplane to target poloidal flux expansion factor. The Eich function is routinely used to describe the heat-flux profile at the tokamak divertor in attached conditions, and provides an approximate relationship between the integrated heat flux width, λ_{int}, and the two fitting parameters λ_q and S [4]

$$\lambda_{int} \approx \lambda_q + 1.64S \quad (2)$$

which quantifies the radial extent on the divertor target over which heat is deposited. As λ_q reduces, particularly in high field devices such as ITER [3,4,5], S may play a greater role in setting the heat-flux profile on the divertor target. It is therefore important to establish the physics underlying S. Upstream transport of particles and heat is mediated, at least in some proportion, by mesoscale turbulent structures termed filaments or blobs [6]. Filament generation and motion is complex, though their relation to profiles in the scrape-off layer can be captured with stochastic models that treat them statistically [7–9]. Transport downstream (encapsulated by S in Eq. (1)) is less well understood. The existence of turbulent fluctuations in the divertor has been demonstrated experimentally with both probe [10,11] and camera based diagnostics [11–13], however no first-principles physics based model for this turbulence presently exists. This paper presents simulations designed to investigate the physics underlying these divertor-localised turbulence processes in a simplified simulation geometry.

2. Simulation setup

The simulation geometry used for this study is a basic field-aligned slab. The x and y dimensions represent the plane perpendicular to the magnetic field and have a well resolved grid resolution with $n_x = n_y = 256$ over a length of $120\rho_s = 43.7$cm. x is the radial coordinate

* Correspondence author.
E-mail address: Nick.Walkden@ukaea.uk (N.R. Walkden).

https://doi.org/10.1016/j.nme.2018.12.005
Received 30 July 2018; Received in revised form 29 November 2018; Accepted 4 December 2018

whilst y is a bi-normal coordinate that is perpendicular to both the radial and field-aligned coordinates. The z dimension represents direction parallel to the magnetic field and, due to the field-aligned nature of scrape-off layer turbulence, has a coarse grid with a large grid spacing of $n_z = 20$ over a lengthscale of $1500\rho_s = 5.46$m. A uniform magnetic field strength of 0.25T and a reference upstream temperature of 40 eV have been used to represent conditions similar to MAST. The magnetic field is approximated here as being straight, though the effect of the magnetic curvature is introduced into the simulations via an effective gravity coefficient defined in refs [14,15,16,17] as $g = 2\rho_s/R_c$ where $R_c = 1.5$m is the radius of curvature. This is similar to the setup often used in isolated scrape-off layer filament simulations. The domain is separated into an 'upstream' source region which occupies the initial 30% of the domain and fuels the divertor volume, and a 'downstream' analysis region. The only difference between the two regions is the presence of axisymmetric density and energy sources in the upstream region. The sources are described by truncated exponential functions such that

$$S_{n,E} = S_{n,E}^{bg} + S_{n,E}^{0} \exp\left(-\frac{x - x_{sep}}{\lambda_{Sn,E}}\right); \quad x \geq x_{sep}$$
$$S_{n,E}^{bg} \quad ; \quad x < x_{sep} \tag{3}$$

where $S_{n,E}^{bg}$ is a small background source used for numerical stability, $S_{n,E}^{0}$ is the peak in the source at the separatrix and $\lambda_{n,E}$ is the e-folding length, chosen such that the profiles at the divertor target at initialization are experimentally realistic. For the simulations presented here the following values have been used: $S_n^0 = 6.03 \times 10^{22} m^{-3}s^{-1}$, $S_n^{bg} = 0.05S_n^0$, $\lambda_{Sn} = 24\rho_s = 8.7cm$: $S_E^0 = 5.8MWm^{-3}$, $S_E^{bg} = 0.005S_E^0$, $\lambda_{SE} = 18\rho_s = 6.6$ cm. Note that these values are taken to be representative of length scales at the divertor entrance, adjacent to the X-point. For representative values at the midplane these values should be divided by 10 to represent flux expansion at the X-point relative to the midplane. The e-folding lengths used in the source profiles provide a midplane $\lambda_q$value of 9 mm for initialization of the simulations presented here, which is within the expected range for MAST L-mode (see Table 1). The energy influx corresponds to an input power of approximately 0.27MW which again is appropriate for Ohmic L-mode in MAST. At the sheath boundary standard sheath boundary conditions are applied (see [14] for a description). In addition, a recycling source exists in the downstream region which recycles 75% of the ion flux that enters the sheath boundary, Γ_{ion}, back up the same magnetic field line instantaneously over an exponential with an e-folding length of 1 m such that

$$S_{rec}(x, z, t) = 0.75\Gamma_{ion}(x, t)\exp(-z). \tag{4}$$

This source attempts to model the recycling of ions from the target heuristically, but does not capture the full interaction between the plasma and a neutral species. An e-folding length of 1 m along the magnetic field line may be interpreted as approximating an ionization mean-free path of approximately 10 cm poloidally in the MAST divertor since the magnetic field is close to toroidal below the X-point. SOLPS simulations of MAST indicate a strong localization of neutral radiation adjacent to the divertor [18] suggesting that 10 cm as a scale length of the recycling source may be realistic. The divertor target boundary condition formally relates to the boundary condition at the magnetic pre-sheath entrance, and is taken here to be normal to the magnetic field. Fig. 1 shows a schematic illustration of the simulation setup.

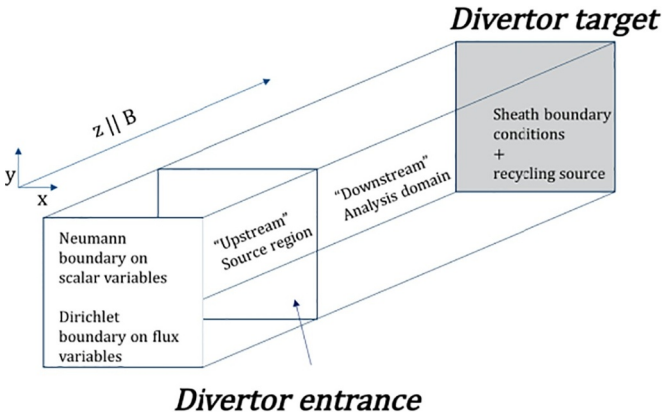

Fig. 1. Schematic illustration of the simulation setup used here to simulate a mock-divertor leg. The upstream source region contains density and temperature sources which fall off radially into the SOL, but are zero in the PFR. The downstream region is where analysis is conducted and represents the divertor volume.

The STORM [14–17] module for BOUT + + [19,20] has been used to conduct these simulations. The module solves a 5-field system of equations for the electron density, n, the electron temperature, T, the electron and ion parallel velocities, V and U respectively, and the vorticity, $\Omega = \nabla_\perp^2\phi$ where ϕ is the electrostatic potential. The potential, ϕ, and conductive parallel heat flux, q_e, are auxiliary variables. The model makes the electrostatic assumption, the cold-ion assumption and the 'Boussinesq' approximation [21]. The full set of equations and their respective boundary conditions at the sheath entrance can be found in [14,17].

To initialize the simulations the code is run in a 2D 'hydrodynamic' mode with $V = U$ imposed and perpendicular diffusion coefficients chosen to be physically realistic. In this case, these were set to be 2.5 times their classical values [22] which corresponds to values of 3.4×10^{-4} and 8.1×10^{-4} times Bohm diffusion for the density and heat diffusivities respectively. These diffusivities are maintained during the turbulent simulations to help stabilize numerical instability. The vorticity is not evolved in hydrodynamic mode and the plasma potential is set by the sheath boundary conditions. This provides the initial conditions for the full 3D turbulent simulations. Fig. 2 shows examples of the hydrodynamic profiles used here as an initial condition, taken at the sheath entrance.

3. Results

3.1. Diagnosing the turbulence

In the initial phases of the simulation, the steep radial profiles that develop from the 2D hydrodynamic initial condition become linearly unstable before developing into fully non-linear turbulence. The linear instability observed to drive the transition into turbulence is the

Table 1
Parameters obtained from an Eich fit of the target heat flux from each of the three simulations. Typical ranges from MAST L-mode data measured by IR thermography [31].

Case	$\lambda_q\,(mm)$	$S(mm)$	$q_0\,(MWm^{-2})$	$q_{bg}\,(MWm^{-2})$	$x_{sep}(m)$
Full	10.46	4.03	5.72	0.044	−0.011
Intr off	7.60	8.31	7.70	0.143	−0.010
KH off	13.00	1.72	4.72	0.043	−0.005
Typical MAST L-mode ranges	7 - 19	2.1 – 5.8	–	–	–

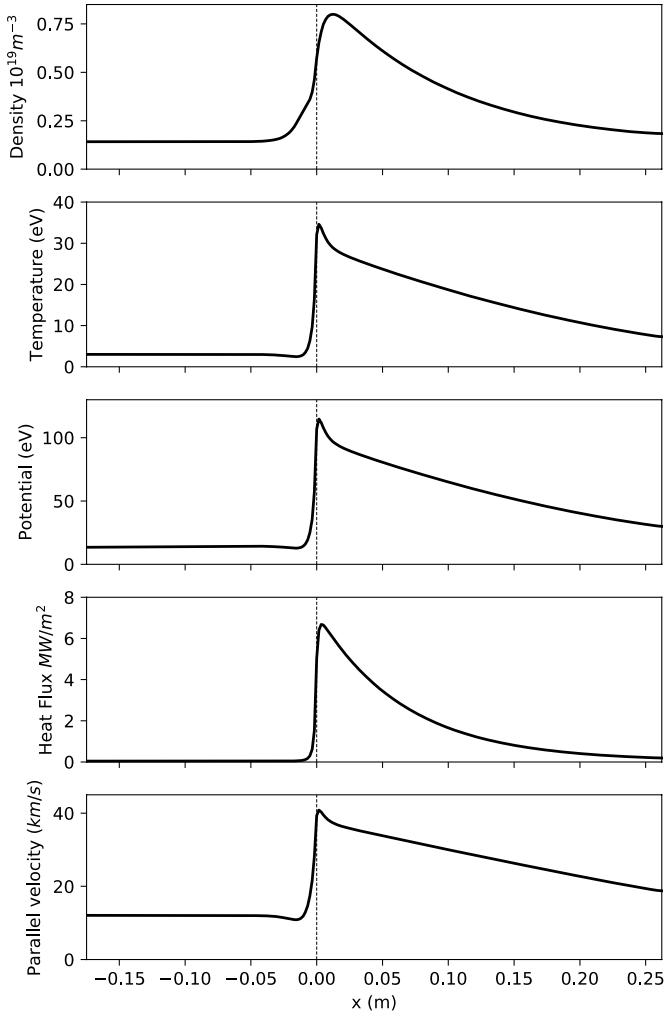

Fig. 2. Radial profiles taken from the 2D 'hydrodynamic' simulation used as an initial condition for turbulence simulations, plotted here at the sheath boundary.

transverse Kelvin–Helmholtz (KH) instability [23]. This is confirmed by calculating the growth rate as a function of $k_\perp$ from the full 3D simulation in an early part of the simulation and comparing to a semi-analytic dispersion relation for the KH instability. Isolating only the non-linearity in the vorticity equation (see [14,17]) and linearizing leads to a generalised eigenvalue equation [24],

$$\frac{\omega}{k_\perp} A(\phi) = B(\phi) \tag{5}$$

$$A \equiv \frac{d^2}{dx^2} - k_\perp^2 \tag{6}$$

$$B \equiv v_E A - v_E^{''} \tag{7}$$

which can be solved for a given $k_\perp$to obtain the complex mode frequency ω of the KH instability. The method is semi-analytic because a second-order finite difference scheme has been used to convert the operators A and B into tri-diagonal matrices. The eigenvalues and eigenvectors of the problem are then computed using the *eigvals* solver in the *scipy.linalg* python library. Fig. 3 shows the dispersion relation from the simulation compared to the semi-analytic prediction.

The comparison between the growthrate calculated in the simulation and semi-analytic case is qualitatively and quantitatively similar, though significant scatter is present in the simulation data. This is likely due to non-linear coupling since, even at early times, many modes are excited by virtue of the broad dispersion relation of the KH instability.

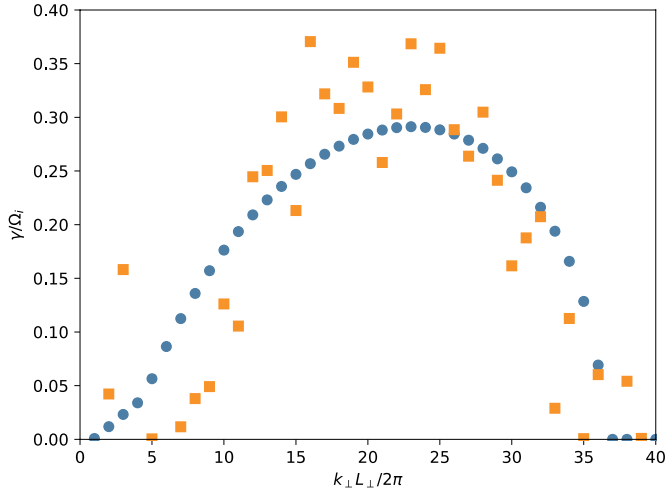

Fig. 3. Dispersion relation from the early phase of the full 3D turbulence simulation (orange squares) compared to the semi-analytic calculation using the averaged potential profile at the divertor target (blue circles) from the 3D simulation. Although there is considerable spread in the simulation results, the dispersion relation is highly consistent with a Kelvin-Helmholtz instability. (For interpretation of the references to color in this figure legend, the reader is referred to the web version of this article.)

It is worth noting that the conditions used for the simulations presented here may be particularly susceptible to the KH instability. In particular, Myra has shown in a recent study [23] that electromagnetic parallel currents and ion diamagnetic effects, both of which were not implemented in the STORM code at the time of this study, may have a stabilizing effect on the KH instability. The former effect requires high values of the plasma β and low values of resistivity so may be less impactful in the tokamak divertor leg. The latter requires gradients in the ion pressure (leading to shear in the ion diamagnetic velocity) to be comparable to the ExB flow shear. In the divertor leg the initial gradient across the separatrix into the PFR, where the KH mode is driven, is determined primarily by the rate of power loss to the target. Since the electron power loss is more rapid than the ion power loss, the electron temperature gradient will likely be steeper than the ion gradient, leading to a steeper ExB velocity shear than the ion diamagnetic velocity shear. As such, both EM and ion diamagnetic effects may impact the stability observed here, but are unlikely to fully stabilize the system.

Although interesting from the perspective of understanding the physics driving the simulation, the linear phase only provides an initial condition for the true saturated turbulence phase, which is of real importance to this study. It is therefore interesting to investigate the role played by the different terms affecting turbulence during the saturated phase. The turbulence drive in the system can be investigated by artificially eliminating different terms in the vorticity equation. To eliminate the KH mechanism, following Ricci and Rodgers [25], the non-linear advection term is modified to

$$[\phi, \nabla_\perp^2 \phi] \rightarrow [\langle\phi\rangle, \nabla_\perp^2 \phi] \tag{8}$$

where $< >$ represents an average in the y direction. Another drive for turbulence is the interchange mechanism [26], which is thought to play a dominant role in the development of turbulence in the upstream SOL [27]. This can be eliminated from the system by setting the effective gravity to zero. Fig. 4 shows cross-sections of the electron pressure and the electrostatic potential at the sheath boundary, compared between three cases: a baseline case (*Full*) where all terms are active, a case where the interchange mechanism is removed (*Intr off*) and a case where the KH mechanism is removed (*KH off*) but the interchange mechanism is retained.

Fig. 4 shows that the KH mechanism and thus KH turbulence is responsible for the formation of a mixing layer around the separatrix

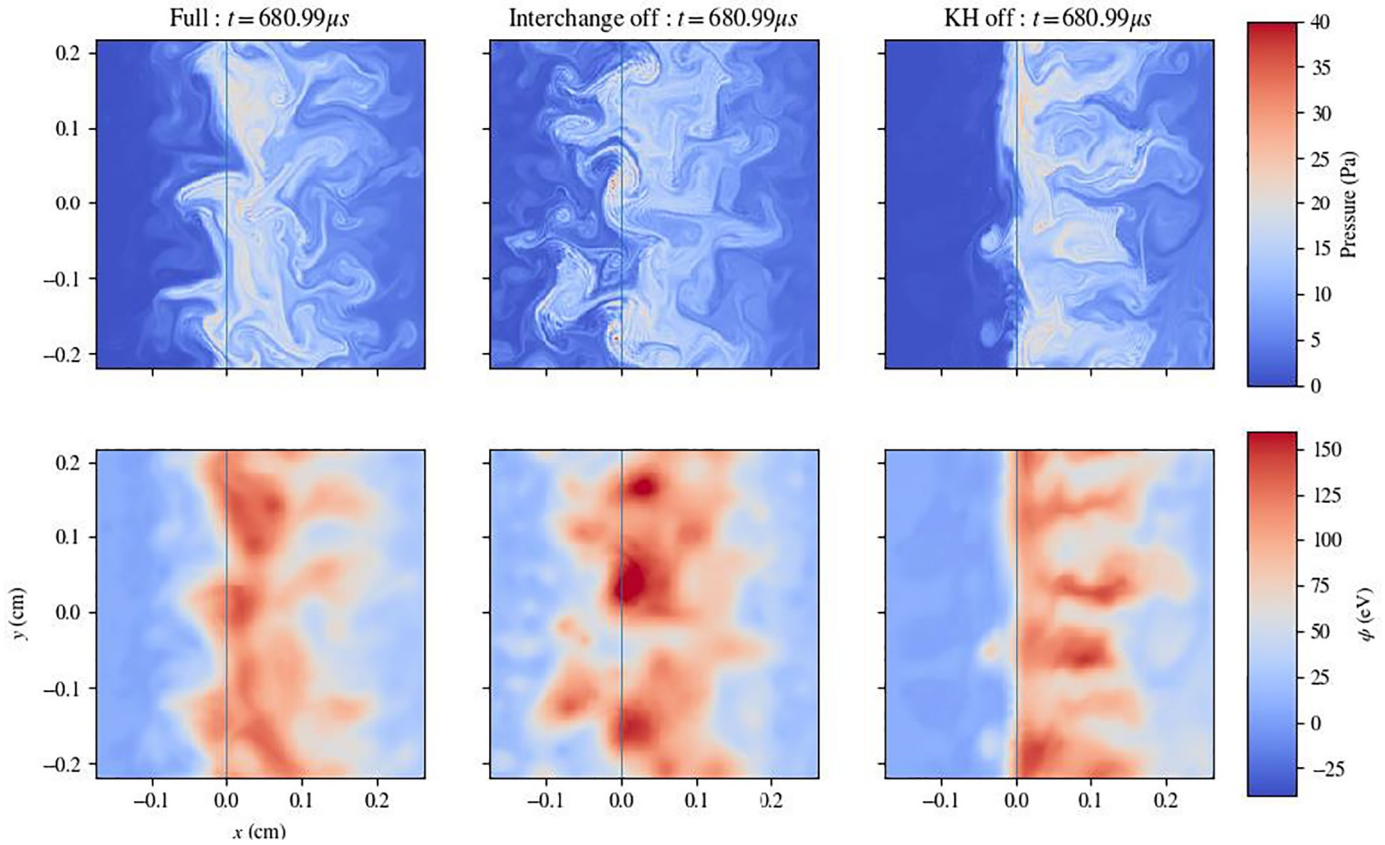

Fig. 4. Cross-sections of the electron pressure (upper) and electrostatic potential (lower) during the saturated turbulence phase compared by the three cases with differing turbulence drives. Cross-sections are taken at the sheath boundary and the separatrix is shown as a vertical dividing line in each cross-section, with the SOL to the right and the PFR to the left.. An animated version of this figure is available at [https://drive.google.com/open?id = 1F2Cda3LpubXT05gaxovyhozrqd0OA9BS].

which relaxes gradients into the PFR region. This is intuitive, since in an outer divertor leg the PFR represents a region of 'good curvature' where the curvature vector is anti-parallel to the pressure gradient, therefore interchange turbulence is not expected to be present. In the SOL, which represents a 'bad curvature' region, some streamer-like structures are present which have a notably longer radial correlation length when the KH mechanism is removed. In a realistic situation turbulence in the far SOL region is strongly coupled to upstream turbulence [11], and therefore the results obtained here in the far SOL region may not be fully relevant to the experimental reality. In the *KH off* case some residual drift-wave turbulence remains local to the separatrix and the simulation does not fully relax to its 2D initial condition. Nevertheless the narrowing of the mixing layer is dramatic. Fig. 5 shows the radial profiles from the turbulent simulations, averaged in time and in the y (bi-normal) direction, at the sheath entrance.

The PFR region of the outer divertor leg is a 'good curvature' region relative to the gradients in the background plasma and is not unstable to interchange turbulence, however when fluctuations are displaced into the PFR they may feel the impact of the magnetic curvature pushing them back towards the separatrix. As such, the interchange mechanism does play a role in the PFR as shown in the comparison between the *Full* and *Intr off* case. Particularly the interchange mechanism leads to a partial narrowing of the profiles into the PFR. Since the linear analysis demonstrated the dominance of the KH instability in the *Full* simulation, and since the PFR is a good curvature region where interchange turbulence would not be expected to develop naturally, this indicates that the role played by the interchange mechanism is prevalent only when turbulence has been established via the KH mechanism.

In Fig. 6 the ExB energy spectrum is compared between the three simulations, where $E(k_\perp)$ is the ExB energy decomposed in $k_\perp$ averaged in y, in time during the saturated turbulence phase and in a small region (~ 2 cm) either side of the separatrix. Fig. 6 indicates that the KH mechanism is responsible for an inverse (enstrophy) cascade [28,29] to larger length scales, limited by transport into the sheath as the turnover time increases in the larger structures. The large-scale structures can then be acted on by the interchange mechanism in a manner similar to filament motion in the upstream SOL [6]. This drives structures that are ejected into the PFR back towards the separatrix leading to the narrowing of the mixing layer. This suggests that the angle of the divertor leg with respect to the curvature vector (which would be parametrised here in the effective gravity) may have an impact on the width of the mixing layer. A divertor leg oriented horizontally in the poloidal plane, which lies parallel to the curvature vector, would be expected to see a reduced impact of the interchange mechanism and thus a widening of the KH mixing layer. This important aspect of these simulations will be followed up in a future report.

3.2. Target heat flux

The width of the mixing layer is echoed in the profile of the electron heat flux (due to the cold ion assumption this is equivalent to the total heat flux in these simulations) at the divertor surface. Fig. 7 shows the electron heat flux (including convective and conductive components) for the three simulation. Also shown are the results from fitting the heat flux with an Eich function (Eq. (1)).

The profile of the heat-flux at the divertor target is well captured by the Eich function. The maximum deviation occurs when the

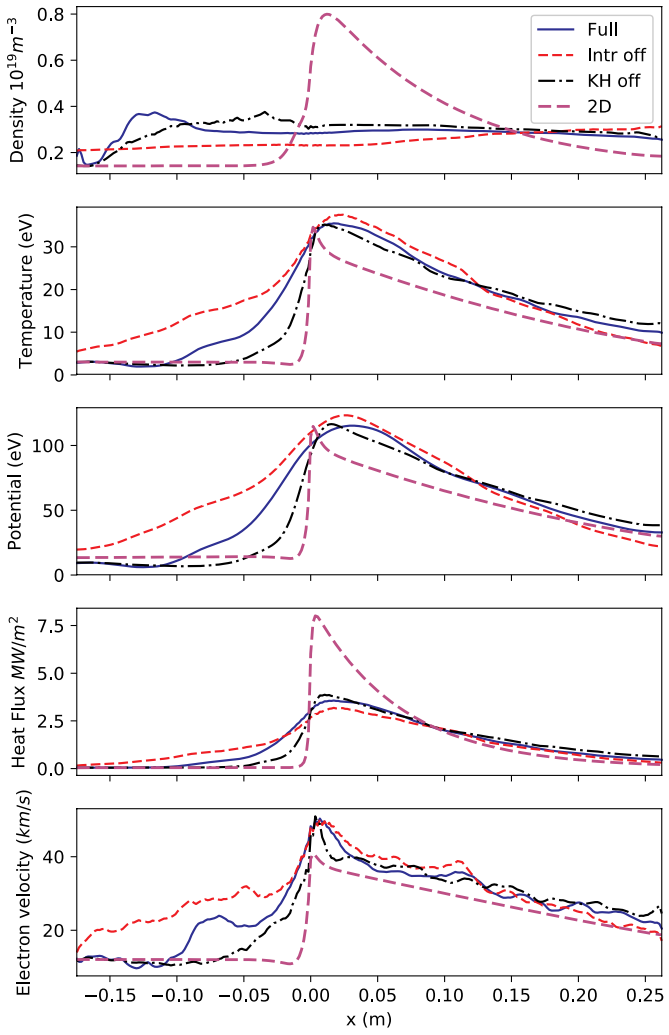

Fig. 5. Radial profiles taken from the three comparison turbulence simulations and the 2D hydrodynamic initial conditions.

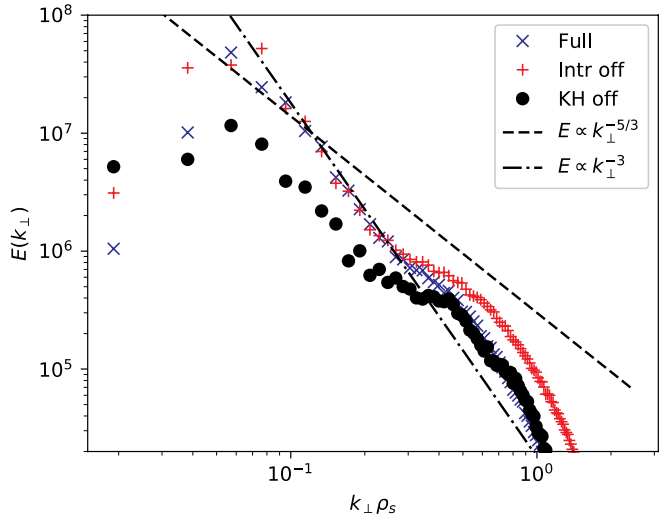

Fig. 6. ExB energy spectrum for each of the three comparison cases. The Kelvin–Helmholtz mechanism is responsible for an inverse cascade towards larger scales. Structure in the tail of the spectrum is partly the result of numerical artefacts which do not affect the transport properties of the simulation.

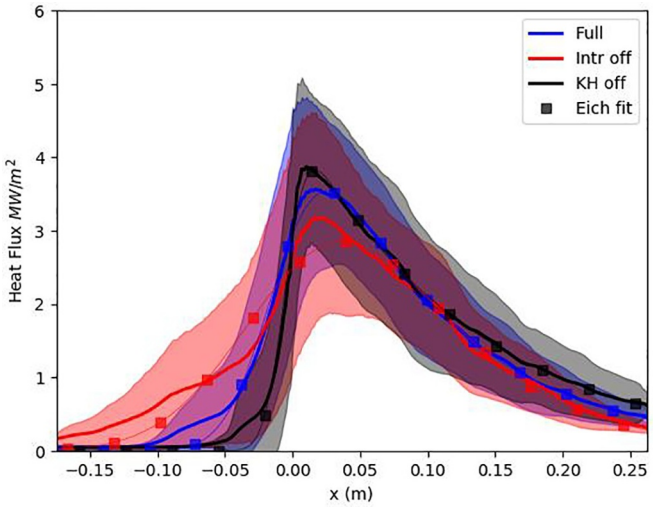

Fig. 7. Heat flux profiles at the sheath boundary for each of the three simulations compared here as bold lines. Square symbols (color coded to their respective profile) show an Eich function fitted to each of the heat flux profiles. The filled areas show one standard deviation either side of the mean profiles due to fluctuations from the turbulence. Fitting parameters are given in Table 1.

interchange mechanism is removed and the KH turbulence is strongest. The deviation from the Eich fit grows in the far PFR, indicating that turbulent transport provides stronger transport into the far PFR than predicted by the simple diffusion-conduction model of the Eich function. In Table 1 the parameters of the Eich fits are given, with a flux expansion factor of $f_x \sim 10$ assumed as a realistic value of poloidal flux expansion for comparison back to the midplane of MAST, in the same manner as Ref. [30].

As expected from the results of the previous section, eliminating the KH turbulence from the system leads to a narrow PFR region and a low value of S, whilst eliminating the interchange mechanism leads to a broad PFR and large values of S. Although, as already stated, the results in the SOL region may not be directly relatable to experimental conditions it is interesting to note that as the PFR narrows the SOL is broadened due to the increased prevalence of interchange turbulence in the SOL region. The *Full* simulation produces a spreading parameter that is within the range measured on MAST [31, 32]. It is also interesting to note that MAST exhibits a larger value of S on the inner target than on the outer [33] experimentally, which is inline with the predictions made here based on the impact of the interchange mechanism on S, since an inner divertor leg will not feel the narrowing effect of the interchange mechanism.

3.3. Transport levels

For each simulation, a representative thermal diffusion coefficient in the radial direction can be obtained by calculating

$$\chi_{eff} \approx \frac{\Gamma_p}{p'} \tag{9}$$

where

$$\Gamma_p = v_{x,ExB} p \tag{10}$$

is the thermal radial ExB flux which is averaged in the y direction and in time, $p = nT$ is the plasma pressure (which is here equivalent to the electron pressure due to the cold ion assumption) and p' is the radial pressure gradient. Fig. 8 shows the measured χ_{eff} in the near-separatrix region of the PFR in both dimensional units and normalised to the Bohm diffusivity, alongside its average in the radial span shown.

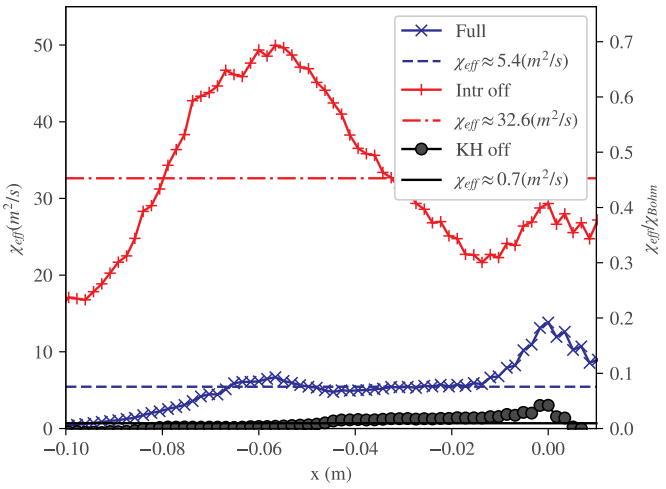

Fig. 8. Effective radial diffusivities from the three comparison simulations in physical dimensions (left axis) and compared to the Bohm diffusivity in the simulations (right axis) in the near-separatrix region of the PFR. Horizontal lines show the average value of the profiles shown for each simulation.

The effective radial thermal diffusivity measured in the *Full* simulation is approximately 10% of the Bohm diffusivity and has a value within the range of diffusivities estimated with target ion saturation current data on MAST [34]. As expected, the *Intr off* simulation shows a much higher effective diffusivity without the interchange mechanism counterbalancing the KH turbulence. The increase in χ_{eff} is around a factor of 6, whilst the increase in S/f_x is much more modest at a factor of 1.9. As the temperature and density in the PFR rise due to the turbulent transport, the heat loss through the sheath also rises because of its dependence on n and T, so the impact on the spreading factor, S/f_x, is reduced.

The effective diffusivity measured in the simulation is certainly not constant radially. A constant diffusion coefficient is a common assumption in axi-symmetric transport modelling of the SOL and it is therefore useful to assess how well such an assumption can capture features of the fully turbulent simulation. To perform this comparison, the code was re-run in hydrodynamic mode (as described in Section 2) using a diffusive transport coefficient of 0.1 χ_{Bohm} for both the particle and thermal diffusivities held constant in the domain. In principle it may be more appropriate to vary these diffusion coefficients in the SOL due to the presence of turbulence from upstream, however the values to set for this diffusion are unclear and somewhat arbitrary. Moreover, far-SOL transport is out of the scope for this study due to its coupling to upstream which is not included in the simulation setup. As a simplifying assumption the diffusion coefficients are therefore fixed. Fig. 9 compares the time and y-averaged profiles of the density, temperature and parallel heat flux between the *Full* turbulent simulation and the hydrodynamic simulation. The profiles are color-coded to their position along the magnetic field line.

Whilst not being able to capture some finer detail of the profile structures, the diffusive approximation does an adequate job of capturing the broadening of the heat flux into the PFR. The temperature in the diffusive simulation has a slightly more relaxed gradient than the turbulent case, whilst the opposite is true for the density. In addition the difference between diffusive and turbulence simulations in the density channels becomes more pronounced further along the magnetic field, as the transport acts to spread the profiles. This may indicate that individual tailoring of the transport coefficients for density and power may improve the agreement, with the method use here underestimating transport of density and overestimating thermal transport in the diffusive simulation. However, the basic features of the profiles are captured by the diffusive simulation, suggesting that, if diffusion coefficients can be appropriately chosen, then the diffusive transport approximation

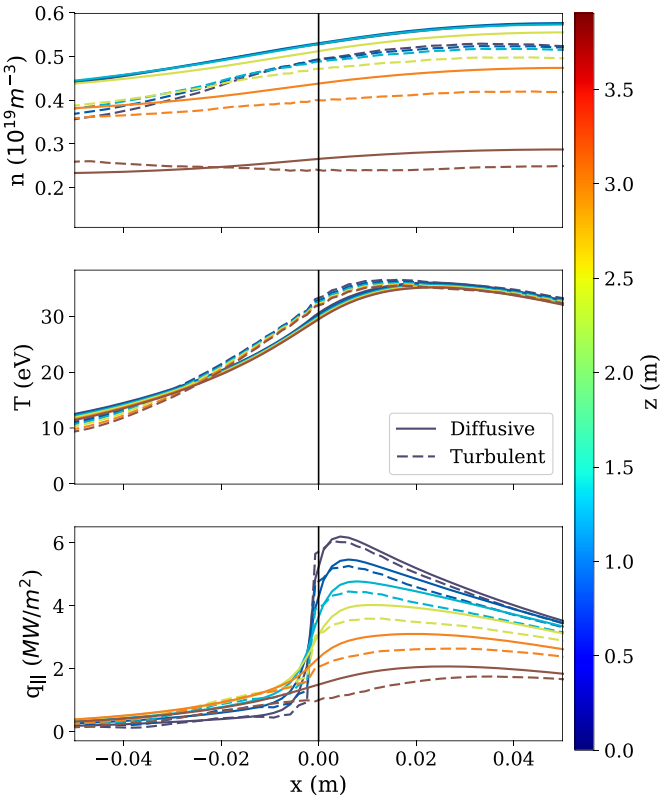

Fig. 9. Comparison of the density, temperature and conductive heat flux steady state profiles between the Full turbulent simulation and a diffusive simulation with a $\chi = 0.1\chi_{Bohm}$. The color coding represents different positions along the magnetic field line from the X-point entrance (Z = 0) to the sheath boundary, and the profiles have been zoomed around the separatrix. .

may be justified in modelling the heat spreading in the divertor leg, at least within the error bounds usually present in 2D transport modelling of the plasma boundary. It is worth noting that this is in stark contrast to the case of the upstream SOL, where cross-field transport is robustly non-diffusive [35, 36]. It is also worth noting that Gallo et al. found no diffusion coefficient in the PFR region in turbulent simulations of TCV using the TOKAM3X code [37]. These simulations were isothermal and may thus miss important physics that contributes to the turbulent processes studied here. Establishing the prominence of the turbulence driven in the rather simplistic geometry used here in fuller (and much more computationally expensive) simulations should be pursued in the future.

4. Summary

This paper has presented simulations of turbulence in a simplified geometry aimed at representing a single isolated tokamak divertor leg using the STORM module of BOUT + + . The simulations are initialised with conditions that satisfy a hydrodynamic steady state with transport coefficients that are near the classical values. These conditions are unstable to a linear Kelvin–Helmholtz instability, though the broad dispersion relation leads to mode coupling even in the early stages of the simulation. In the saturated turbulence phase the turbulence is sustained by the Kelvin–Helmholtz mechanism. This is demonstrated by comparing simulations with both the Kelvin–Helmholtz and interchange mechanism artificially removed in turn. The interchange mechanism has a regulatory effect on the turbulence by acting on large scale structures that appear in the PFR due to the turbulence and driving them back towards the SOL. The heat flux profiles at the divertor target produced from the full simulation show spreading into the private-flux region that is comparable to experimental ranges measured

on MAST. Effective transport coefficients are estimated from the simulation in the near-separatrix region of the PFR and are approximately $\chi \approx 0.1\chi_{Bohm}$, again within the range of experimental estimates for MAST. Finally a diffusive, axisymmetric simulation is run with these transport coefficients used and the resulting profiles are similar to the time and poloidally averaged profiles from the turbulent simulation, though some finer details in the profiles are not recovered. This suggests that in the divertor volume, the diffusive approximation may be adequate for capturing the important aspects of radial transport due to turbulence, in contrast to upstream SOL turbulence which is robustly non-diffusive.

Acknowledgements

This work has been carried out within the framework of the EUROfusion Consortium and has received funding from the Euratom Research and Training Programme 2014–2018 under grant agreement No 633053 and from the RCUK Energy Programme [grant number EP/P012450/1]. NRW gratefully acknowledges funding and support through EUROfusion researcher grant AWP16-ERG-CCFE/Walkden. The simulations presented here were carried out on the CINECA Marconi supercomputer under the SOL_BOUT project. To obtain further information on the data and models underlying this paper please contact PublicationsManager@ccfe.ac.uk. The views and opinions expressed herein do not necessarily reflect those of the European Commission.

Supplementary materials

Supplementary material associated with this article can be found, in the online version, at doi:10.1016/j.nme.2018.12.005.

References

[1] R. Schneider, et al., Plasma Edge Physics with B2-EIRENE, Contrib. Plasma Phys. 46 (2006) 3.
[2] E. Havlickova, W. Fundamenski, F. Subba, D. Coster, M. Wischmeir, G. Fishpool, Benchmarking a 1D scrape off layer code SOLF1D with SOLPS and its use in modelling long legged divertors, Plasma Phys. Control. Fusion 55 (2013) 065004.
[3] T. Eich, A.W. Leonard, R.A. Pitts, et al., Scaling of the tokamak near the scrape-off layer H-mode power width and implications for ITER, Nucl. Fusion 53 (2013) 093031.
[4] M.A. Makowski, D. Elder, T.K. Gray, et al., Analysis of a multi-machine database on divertor heat fluxes, Phys. Plasmas 19 (2012) 056122.
[5] T. Eich, B. Sieglin, A. Scarabosio, et al., Inter-ELM power decay length for JET and ASDEX Upgrade: measurement and comparison with heuristic drift-based model, Phys. Rev. Lett. 107 (2011) 215001.
[6] D.A. D'Ippolito, J.R. Myra, S.J. Zweben, Convective transport by intermittent blob-filaments: Comparison of theory and experiment, Phys. Plasmas 18 (2011) 060501.
[7] F. Militello, J.T. Omotani, Scrape off layer profiles interpreted with filament dynamics, Nucl. Fusion 56 (2016) 104004.
[8] F. Militello, J.T. Omotani, On the relation between non-exponential scrape off layer profiles and the dynamics of filaments, Plasma Phys. Control Fusion 58 (2016) 125004.
[9] F. Militello, T. Farley, K. Mukhi, N.R. Walkden, J.T. Omotani, A two-dimensional statistical framework connecting thermodynamic profiles with filaments in the scrape off layer and application to experiments, Phys. Plasmas 25 (2018) 056112.
[10] I. Garcia-Cortes, et al., Characterization of fluctuations in the JET divertor plasmas with Langmuir probes, Plasma Phys. Control Fusion 38 (1996) 2051.
[11] N.R. Walkden, J. Harrison, S.A. Silburn, et al., Quiescence near the X-point of MAST measured by high speed visible imaging, Nucl. Fusion 57 (2017) 126028.
[12] J.R. Harrison, G.M. Fishpool, A.J. Thornton, N.R. Walkden, The appearance and propagation of filaments in the private flux region in Mega Amp Spherical Tokamak, Phys. Plasma 22 (2015) 092508.
[13] R.J. Maqueda, D.P. Stotler, Intermittent divertor filaments in the national spherical torus experiment and their relation to midplane blobs, Nucl. Fusion 50 (2010) 075002.
[14] N.R. Walkden, L. Easy, F. Militello, J.T. Omotani, Dynamics of 3D isolated thermal filaments, Plasma Phys. Control Fusion 58 (2016) 115010.
[15] L. Easy, F. Militello, J.T. Omotani, Three dimensional simulations of plasma filaments in the scrape off layer: A comparison with models of reduced dimensionality, Phys. Plasmas 21 (2014) 122515.
[16] J.T. Omotani, F. Militello, L. Easy, N.R. Walkden, The effects of shape and amplitude on the velocity of scrape-off layer filaments, Plasma Phys. Control Fusion 58 (2016) 014030.
[17] F. Militello, N.R. Walkden, T. Farley, et al., Multi-code analysis of scrape-off layer filament dynamics in MAST, Plasma Phys. Control Fusion 58 (2016) 105002.
[18] E. Havlickova, J. Harrison, B. Lipschultz, et al., SOLPS analysis of the MAST-U divertor with the effect of heating power and pumping on the access to detachment in the Super-x configuration, Plasma Phys. Control Fusion 57 (2015) 115001.
[19] B.D. Dudson, et al., BOUT++: A framework for parallel plasma fluid simulations, Comput. Phys. Commun. 180 (2009) 1467.
[20] B.D. Dudson, et al., BOUT++: Recent and current developments, J. Plasma Phys. 81 (2015) 1.
[21] J.R. Angus, M.V. Umansky, Modeling of large amplitude plasma blobs in three-dimensions, Phys. Plasma. 21 (2014) 012514.
[22] S.I. Braginskii, Rev. Modern Phys. 1 (1965) 205 New York: Consultants Bureau.
[23] J.R. Myra, D.A. D'Ippolito, D.A. Russell, M.V. Umansky, D.A. Baver, Analytical and numerical study of the transverse Kelvin–Helmholtz instability in tokamak edge plasmas, J. Plasma Phys 82 (2016) 905820210.
[24] K. Lotov, D. Ryutov, J. Weiland, Velocity shear effects in the problem of the electron temperature gradient instability induced by conducting end-walls, Physica Scripta 50 (1994) 153–160.
[25] B.N. Rogers, P. Ricci, Turbulence phase space in simple magnetized toroidal plasmas, Phys. Rev. Lett. 104 (2010) 225002.
[26] O.E. Garcia, N.H. Bian, W. Fundamenski, Radial interchange motions of plasma filaments, Phys. Plasmas 13 (2006) 082309.
[27] O.E. Garcia, V. Naulin, A.H. Nielsen, J. Juul Rasmussen, Computations of intermittent transport in scrape-off layer plasmas, Phys. Rev. Lett. 92 (2004) 165003.
[28] R.H. Kraichnan, Inertial ranges in twodimensional turbulence, Phys. Fluids 10 (1967) 1417.
[29] R.H. Kraichnan, D. Montgomery, Two-dimensional turbulence, Rep. Prog. Phys 43 (1980) 548.
[30] D. Moulton, J. Harrison, B. Lipschultz, D. Coster, Using SOLPS to confirm the importance of total flux expansion in Super-X divertors, Plasma Phys. Control. Fusion 59 (2017) 065011.
[31] S. Elmore, et al., Scaling of the scrape-off layer width in MAST L-mode plasmas as measured by infrared thermography, Proceedings of the 45th EPS Conference on Plasma Physics, Prague, 2018.
[32] A.J. Thornton, A. Kirk, Scaling of the scrape-off layer width during inter-ELM H modes on MAST as measured by infrared thermography, Plasma Phys. Control Fusion 56 (2014) 055008.
[33] F. Militello, et al., Characterisation of the L-mode scrape off layer in MAST: decay lengths, Nucl. Fusion 56 (2015) 016006.
[34] J. Harrison, G.M. Fishpool, A. Kirk, L-mode and inter-ELM divertor particle and heat flux width scaling on MAST, J. Nucl. Mater. 438 (2013) S375.
[35] O.E. Garcia, et al., Turbulent transport in the TCV SOL, J. Nucl. Mater. 363 - 365 (2007) 575.
[36] V. Naulin, et al., Turbulent transport and the plasma edge, J. Nucl. Mater. 363 – 365 (2007) 24.
[37] A. Gallo, et al., Impact of **the plasma**geometry on divertor power exhaust: experimental evidence from TCV and simulations with SolEdge2D and TOKAM3X, Plasma Phys. Control Fusion 60 (2018) 014007.